Characterising the flow-boundary zone in fluidised granular currents

Gregory M Smith, School of Environmental Sciences, University of Hull, UK

Rebecca Williams, School of Environmental Sciences, University of Hull, UK

Pete Rowley, Department of Geography and Environmental Sciences, University of the West of England, UK[1]

Dan Parsons, Energy and Environment Institute, University of Hull, UK[2]

*greg.m.smith91@gmail.com @GregMSmith91

This is a non peer-reviewed preprint submitted to EarthArXiv. This manuscript has been submitted to the Journal of Geophysical Research: Solid Earth.

Twitter Handles -

GS: @GregMSmith91

RW: @Volcanologist

PR: @OrbitalPete

DP: @bedform

[1] Current affiliation School of Earth Sciences, University of Bristol, UK

[2] Current affiliation Loughborough University, UK

Characterising the flow-boundary zone in fluidised granular currents

Gregory M Smith, School of Environmental Sciences, University of Hull, UK

Rebecca Williams, School of Environmental Sciences, University of Hull, UK

Pete Rowley, Department of Geography and Environmental Sciences, University of the West of England, UK[3]

Dan Parsons, Energy and Environment Institute, University of Hull, UK[4]

[3] Current affiliation School of Earth Sciences, University of Bristol, UK

[4] Current affiliation Loughborough University, UK

Key Points

- High velocity video and use of tracking particles allows identification of the flow boundary-zone (FBZ) in defluidising granular currents.
- Law of the wall calculations are applied to explore possible shear values in the currents as they deposit a sequence of steepening bedforms.
- Velocity and shear parameters in the currents can be related to non-depositional/depositional regimes, and distinct bedform morphologies.

Abstract

Pyroclastic Density Currents (PDCs) are hazardous flows of hot gas and volcanic particles which have a diverse range of flow behaviours and depositional mechanisms. Here we use defluidising granular currents, analogous to dense PDCs, to examine the region known in the volcanological literature as the flow-boundary zone. This consists of the lower part of the current and upper part of its aggrading deposit, and its behaviour is thought to control the characteristics of the deposit, independent of bulk current conditions. In these experiments we define the top of the flow-boundary zone as equal to the top of the exponential tail of the velocity profile through the current. Using part of the viscous law of the wall to acquire estimates of shear velocity and shear stress it is shown how variations in parameters in the flow-boundary zone control deposition. In waning currents, the flow-boundary zone transitions from thin, high-shear granular-flow dominated, to thick, low-shear fluid-escape dominated, during the deposition of a sequence of steepening bedforms. This process results in inverse grading at the base of

the deposit as initial high shear allows effective vertical particle segregation. Attention is also drawn to how the near-wall viscous sublayer of turbulent fluid flows is analogous to the flow-boundary zone in granular currents. This work demonstrates that the deposits of defluidising granular currents are controlled by the characteristics of the flow-boundary zone, as well as factors such as the current's response to topography.

Plain Language Summary

Explosive volcanic eruptions can generate phenomena called pyroclastic density currents – avalanches of hot gases and rock which pose great threat to life due to their high speeds, high temperatures, and unpredictable behaviour. The physics of PDCs are poorly understood, due in part to the difficulty of observing and measuring them in the field. Analogue laboratory experiments can be useful in simulating replica currents under controlled conditions, allowing us some insight into the processes and mechanisms which may be taking place in natural PDCs. Here we show that the flow-boundary zone (FBZ), a concept used by field volcanologists to interpret PDC deposits, is identifiable in these experimental currents based on variations of their velocity profiles, and that the characteristics of the FBZ change as various bedforms are deposited. Understanding the depositional behaviour of PDCs is crucial to effective hazard assessment and correctly interpreting the deposits of past currents.

1. Introduction

Pyroclastic density currents (PDCs) are hot mixtures of gas and volcanic particles commonly generated during explosive volcanic eruptions. Their ability to travel at high speeds over large distances makes them a deadly natural hazard (Sulpizio et al., 2014). PDCs range on a spectrum from dense to dilute (Branney & Kokelaar, 2002), and both dense and dilute particle support mechanisms can exist simultaneously in the same current (Breard et al., 2016). Even high concentration PDCs, however, are unusually mobile (Calder et al., 1999; Hayashi & Self, 1992) due to the presence of high gas pore pressures (e.g. Breard et al., 2019; Lube et al., 2019; Roche, 2012) which decrease frictional forces between particles.

PDCs deposit by progressive aggradation, where deposits form by the sustained build up of particles sedimenting from the lower boundary of the current (Branney & Kokelaar, 1992; Breard et al., 2017; Calabrò et al., 2022; Fisher, 1966). Hence, the characteristics of the region adjacent to the boundary, the flow-boundary zone, control the characteristics of the resulting deposit (Branney & Kokelaar, 2002; Sulpizio & Dellino, 2008; Zrelak et al, 2020). For example, a moderate-high concentration 'granular flow-dominated' flow-boundary zone deposits massive lithofacies. Conversely, stratification is usually thought to be the result of deposition from low concentration 'traction-dominated' flow-boundary zones (Branney & Kokelaar, 2002). Although the presence of stratification and bedforms in PDC deposits has traditionally been ascribed to deposition from low concentration PDCs, recent experimental work (Rowley et al., 2014, 2023; Smith et al., 2020) has shown that structures with complex internal surfaces can be deposited from dense granular currents when fluidised.

1.1 Definitions used for the velocity profile and the flow-boundary zone

All terms used herein are defined in Table 1. Velocity profiles of depositing granular currents typically have a concave down, exponential tail close to zero velocity and a quasi-linear region leading up to maximum velocity (e.g. Farin et al., 2014; Forterre & Pouliquen, 2008; GDR MiDi, 2004; Lube et al., 2007; Mangeney et al., 2010; Wang et al., 2019). Much less work has been done on dense granular currents in which the interstitial fluid plays an important role, although velocity profiles of fluidised granular currents have been described before (e.g. Breard & Lube, 2017; Girolami et al., 2010; Jessop et al., 2017; Roche et al., 2010). Typically these profiles show that velocity is non-zero at the base of the current and increases either linearly or concave-up towards the free surface, although maximum velocity may be lower than this. An exponential tail, however, is not recognised.

Here, the flow-boundary zone is defined as the basal region showing increasing acceleration with height from the top of the static deposit (concave-down curve in Fig. 1), which is distinct from the quasi-linear velocity increase with height above this. Because the particle concentration in the current and deposit is similar, and due to the extremely slow motion of particles towards the base of the exponential tail of the velocity profile, it is not feasible to define the base of the current/top of the static deposit as the point of zero velocity. Instead this boundary is defined as the point at which the velocity is 1% of the maximum velocity of that profile. A similar concept was used successfully for dense granular currents by Wang et al. (2019). The flow-boundary zone, then, includes the lower region of the current, as well as the mobile portion of the deposit. The (quasi) linear region of the velocity profile, which typically becomes concave-up close to maximum velocity (U_{max}), is referred to as the granular flow (Fig. 1). This is bounded at the top by the free surface and the transition to the dilute cloud, however this study focuses on the dense granular current and does not consider the area above U_{max}. U_{max} is used instead of surface velocity as in many other studies on granular currents because in the dense regions of PDCs U_{max} can be below the free surface.

Here the evolution of velocity profiles of a fluidised granular current from its non-depositional phase through deposition of various bedforms is reported. PIV analysis allows the imaging of the flow-boundary zone and the identification of an exponential tail in the velocity profiles of the depositional phase, showing that i) a flow-boundary zone exists and ii) there is no definitive boundary between current and deposit. The law of the wall for the viscous sublayer is then applied to obtain shear velocity and shear stress data and describe how changing parameters in the flow-boundary zone affect the characteristics of the deposit, as well granular segregation processes.

2 Methods

2.1 Experimental Method

The experimental flume described in Smith et al. (2020) is used to simulate dense, granular PDCs and the formation of their deposits. The base of the flume comprises one-meter long sections which can provide independently controlled gas fluxes through a porous baseplate in each section in order to fluidise any overpassing material. The flume was kept at an angle of 2°, to promote flow away from the impingement surface while maintaining a sub-horizontal surface.

The air-supply plumbing allows a gas flux to be fed through the base of the flume, producing sustained aeration of the current. In such thin (<0.03 m), rapidly degassing laboratory currents, this enables the simulation of the long-lived high gas pore pressures that characterize thicker PDCs (Rowley et al., 2014; Smith et al., 2018, 2020). Deposition was triggered by the absence of the gas flux in the second and third chambers of the flume. The first chamber always had a gas flux of 0.93 U_{mf_st}, so that experimental currents experienced significant deaeration after passing into the second chamber of the flume.

Experiments were recorded using a high-speed camera at 800 frames per second. This video recorded a side-wall area of the channel at 1 m runout (across the contact between the first and second gas supply chambers), allowing for measurement of the conditions within the current. From the opening of the trapdoor to the cessation of deposition in the target area each experimental run lasted three to four seconds.

The experiments were performed using particles of spherical soda lime ballotini. The grain size distribution was bimodal, with one population of 45-90 µm (average δ_{32} = 63.4 µm calculated from six samples across the material batch) similar to the particles used in previous experimental granular currents (e.g. Montserrat et al., 2012; Roche et al., 2004; Rowley et al., 2014; Smith et al., 2018, 2020). In order to accurately measure parameters within the current, larger tracking particles, dyed black, were added to the sediment charge. This second population of 150-250 µm diameter particles comprised ~15% of the current. The 45-90 µm ballotini belong to the Group A classification of Geldart (1973), comprising particles which expand homogenously above U_{mf} until bubbles form, and which are non-cohesive. The fraction > 200 µm belongs to group B, where particles are less able to sustain a pore pressure (Roche et al., 2004), but this is only a small percentage of the entire particle mass. These particles do not affect the bulk Group A behaviour, as demonstrated in Roche et al. (2006); when the Group A fraction is >0.5 the whole current experiences Group A behaviour. As PDCs contain dominantly Group A particles, this allows dynamic similarity between the natural and experimental currents (Roche, 2012), ensuring that the experimental currents do not allow gas to escape too readily as would occur if the majority of particles were too cohesive or too coarse (Druitt et al., 2007). Detailed mechanical properties of the 45-90 µm particles are given in Smith et al. (2020).

The results reported here are taken from one experimental run (Movie M1). To test repeatability, the thickness of the deposit+current was measured from the base of the flume in five locations at four different points in time, for four separate currents. Analysis of Variance (ANOVA) tests show that for three of these points in time, the mean deposit+current thickness over all locations was similar across the repeats ($P > 0.05$). Raw data is presented in Supplementary Table S1, and a visual comparison in Supplementary Figure S1. Only at 0.2 seconds was there a significant difference, due to current c being thinner at this point. As this is very soon after propagation began it is likely this difference in thickness resulted from unsteadiness caused by the initial impingement of the charge onto the base of the flume. Given the high P-values for the majority of the repeats it is reasonable to conclude that at a given point in time the average thickness of the current and its deposit does not vary significantly over multiple runs, variation over time is systematic and reproducible, and therefore the experimental run reported here is representative of its conditions.

2.2 Analytical Method

PIV analysis was carried out using the PIVlab toolbox for Matlab (Thielicke, 2014; Thielicke & Stamhuis, 2014), using the Fast-Fourier Transform (FFT) window deformation algorithm. This algorithm has been demonstrated to work in granular materials (Sarno et al., 2018). Pixel (px) size in the analysed video frames was 9E-05 m, giving 1 px per frame = 0.07 m/s. Each analysis used four passes, with the interrogation window decreasing from 64 px in the first pass to 50 px, 36 px, and 22 px in the final pass. Using interrogation windows smaller than 22 px resulted in a very low signal to noise ratio. In a multi-pass analysis the interrogation window of the first pass should be three to four times the size of the maximum displacement between frames in order to reduce error (Sarno et al., 2018). As the vast majority of displacements in these granular currents are less than ~20 px (i.e. 1.4 m/s) this yields acceptable results.

Each analysis consisted of averaging five frames from the high speed video to generate a velocity field (e.g. Fig. 2). Profiles of velocity magnitude were taken perpendicular to the free surface, and exported for analysis (e.g. Fig. 3). Data points above a current's U_{max} were not analysed except to calculate current thickness.

3 Results

3.1 Velocity fields and profiles

Deposits formed by the experimental granular currents were similar to those formed in the experiments described in Smith et al. (2020). The formation of bedforms is marked by either diffuse stratification or by the angle of the surface of the aggrading deposit. Three types of bedform are identified: i) planar/very shallow backset (<2°) bedsets (Fig. 3b), ii) backset bedforms with shallow stoss sides less than the dynamic angle of repose ($< \Theta_{Dyn}$, Fig. 3c), and iii) backset bedforms with steep ($>\Theta_{Dyn}$) stoss sides (Fig. 3d).

Figure 2 shows representative velocity fields for the non-depositional phase of the current (Fig. 2a), and for the current during the deposition of planar, shallow, and steep bedforms (Fig. 2b-d). Figure 3 shows representative velocity profiles generated at regular intervals from the velocity fields, superimposed over video frames for the non-depositional phase of the current (Fig. 3a), and for the current during the deposition of planar, shallow, and steep bedforms (Fig. 3b-d). Further examples of velocity profiles can be found in the Supplementary Figures S2-S13.

Velocity profiles from the non-depositional phase of the current consist of one or two quasi-linear gradients leading up from non-zero velocity at the base to U_{max}. Velocity profiles from close to the head of the current are very linear. There is occasionally a very small concave-down zone at the base of the velocity profiles from the non-depositional phase. The mean slip at the base of the non-depositional current is 0.46 m/s. Where the velocity profile consists of more than one quasi-linear gradient the upper one is considerably steeper, sometimes almost vertical (Fig. 3a). This is similar to the velocity profiles through the non-expanded fluidised granular currents of Girolami et al. (2010) and velocity profiles through the basal granular-fluid flow of Breard and Lube (2017). In Figure 3a, the two gradients are approximately concordant with inverse grading within the current, with almost uniform velocity in the coarser part of the current. The velocity profiles seen in the depositing phases of the current, meanwhile, generally consist of a concave down zone, with an exponential tail tending towards zero, and a quasi-linear or concave up profile leading to U_{max} above this (Fig. 3b-d).

Within the granular current, U_{max} decreases with increasing steepness of the bedforms being deposited (see also Smith et al. 2020). The gradient of the velocity profiles below U_{max} for the current in its depositional phase increases with increasing bedform steepness. The position of U_{max} as a proportion of current thickness (H) varies. Expressed as (H-Y')/H, the average position of U_{max} across all phases of deposition is 0.76, but it can be lower than this, especially during the deposition of planar bedforms, where over 25% of recorded U_{max} were below 0.6 (ranges are plotted in Fig. 5.4a). When the current is non-depositional or depositing shallow bedforms, U_{max} in velocity profiles is close to the free surface. The outliers in the non-depositional dataset are from less than 0.03s after the passage of the leading edge of the current. Velocity profiles from when the current is depositing planar bedforms show the most complexity and often have two velocity peaks, with U_{max} either very close to the free surface or ~60% of current thickness, resulting in a range from 0.57-1. For velocity profiles from when the current is depositing steep bedforms U_{max} is ~75% of current thickness, and has the most restricted range, of 0.61-0.83.

3.2 Quantifying the flow-boundary zone

3.2.1 By velocity profile

The top of the flow-boundary zone at any given point in the current is here defined as the inflection point at which the velocity profile first begins to deviate (concave down) from the quasi-linear portion of the profile – the granular flow (see Fig. 1) – assuming that this point is both < 50% U_{max} and that the angle between the gradients is > 5°. This is to ensure that the flow-boundary zone top is chosen based on perturbations related to deposition of particles, and not minor fluctuations in velocity within the granular flow, or larger fluctuations more closely associated with U_{max}. No flow-boundary zones were defined for the non-depositional phase of the current; even where small concave down regions were present at the base of velocity profiles, because the base of the current at this point is travelling at far greater than zero velocity. The velocity within the flow-boundary zone generally tends exponentially towards zero, but when the current is depositing planar bedforms velocity may actually increase towards the current base (e.g. profile at 98 cm in Fig. 3b). As the current is still travelling relatively fast when depositing planar bedforms velocity rarely decreases to 1% of U_{max}, meaning that at many points the whole deposit is technically part of the flow-boundary zone although stationary to the naked eye.

Figure 4b shows the ranges of the thickness of the flow-boundary zone for velocity profiles of the current when depositing planar, shallow, and steep bedforms as a proportion of the current thickness (H-Y'/H). The thickness of the flow-boundary zone increases slightly from the deposition of planar to shallow bedforms and significantly from the deposition of shallow to steep bedforms: the interquartile ranges of the shallow and steep bedform datasets do not overlap. Despite the small increase in flow-boundary zone thickness from deposition of planar to deposition of shallow bedforms, the flow-boundary zone of the current during deposition of shallow bedforms has a much greater range of thicknesses than during deposition of planar bedforms (0.05-0.4 compared to 0.12-0.32).

3.2.2 Application of the viscous Law of the Wall

Field studies have inferred that shear intensity in the flow-boundary zone is an important control on deposit characteristics (Branney & Kokelaar, 2002; Pollock et al., 2019; Sulpizio et al., 2014; Zrelak et al., 2020), but absolute values of shear parameters are difficult to establish from interpretation of deposits. Here this control is quantified by calculating shear velocity and shear stress values by treating the dense granular current as analogous to the wall-adjacent viscous sublayer in clean-water channel currents.

The Law of the Wall is used for estimating the velocity of turbulent (high *Re*) flow, parallel to the wall (or current base). The Reynolds Number (*Re*) is the ratio of inertial to viscous forces and can be expressed as:

$$Re = \frac{U\rho H}{\mu} \qquad \text{(Eq. 1)}$$

where U is velocity, ρ is density, H is current thickness, and μ is viscosity. For these experimental currents, using bulk current values of U = 0.5 m/s, H = 0.01 m ρ = 2500 kg/m^3, and μ = 167 Pa gives *Re* = 0.075, significantly below the laminar-turbulent transition and demonstrating the clear dominance of viscous forces. Bulk ρ and μ values were calculated following Wohletz (1998), using a ρ_f of 1.225. The small scale of these experimental currents contributes to the very small *Re*, which is less than what would be expected in natural granular currents. In natural PDCs, typical U and H values range from 5-30 m/s and 1-50 m respectively (Roche, 2012). However even scaling the velocity and thickness up by a factor of 10 towards these more realistic values results in *Re* = 7.5, still far below the turbulent zone.

The viscous sublayer is the portion of the velocity profile in aqueous systems where viscous forces dominate. It can be estimated using part of the Law of the Wall expressed as follows:

$$\frac{\underline{U}}{U^*} = \frac{\rho_f U^* Y}{\mu_f} \qquad \text{(Eq. 2)}$$

where $\underline{U}$ is the time-averaged velocity, U* is shear velocity, ρ_f is fluid density, μ_f is fluid viscosity and Y is distance from the current base (Southard, 2006). It can also be expressed as:

$$U^+ = Y^+ \qquad \text{(Eq. 3)}$$

where dimensionless velocity U^+ = U/U* and dimensionless distance from the current base $Y^+ = (\rho_f U^* Y)/\mu$. Y^+ can also be written as:

$$Y^+ = \frac{U^* Y}{V} \qquad \text{(Eq. 4)}$$

where V is the kinematic fluid viscosity, μ_f/ρ_f.

Equation 2 is only applicable in the viscous sublayer, where $Y^+ < 5$. However due to the very low *Re* of these experimental granular currents it is likely to be valid throughout their thickness and provide a better approximation than the standard Law of the Wall. It must be noted, however, that Equation 2 is derived for dynamically smooth flow and that it may not be applicable to two-phase flow which is dynamically rough. Hence, the equation has been applied here purely to explore possible values of shear velocity and shear stress, and to show general current behaviour across the experiment, and is not validated.

Equation 2 can be rearranged to provide shear velocity U*:

$$U^* = \sqrt{\frac{U\mu_f}{Y\rho_f}} \qquad \text{(Eq. 5)}$$

and as shear stress τ is related to U* the following equation can then be used:

$$\tau = {U^*}^2 \rho_f \qquad \text{(Eq. 6)}$$

Figure 5 shows calculated U* and τ values for velocity profiles of the current during different stages of deposition. Values are presented as depth-averaged throughout the flow-boundary zone (Fig. 5d), the granular flow (Fig. 5c), and both together (Fig. 5a), as well as the basal values from the flow-boundary zone (Fig. 5f) and the granular flow (Fig. 5e) in depositional currents, and basal values from the non-depositional phase of the current (Fig. 5b).

Shear velocity and shear stress calculated as depth-averaged values for the whole velocity profile below U_{max} are higher in the non-depositional phase than in the depositional phases (Fig. 5a). The general trend shows that as U* and τ in both the granular flow and the flow-boundary zone decrease as the current begins to deposit. As the current wanes and deposits bedforms of increasing steepness, U* and τ continue to decrease.

Depth-averaged U* and τ in the flow-boundary zone are lower than depth-averaged granular flow values (Fig. 5c and 5d). Planar bedforms are deposited when the current has high U* and τ (Fig. 5a, d and f) and a thin flow-boundary zone (Fig. 4b), where shear is noticeably higher at the base (Fig. 5f). Further decreases in U* and τ result in the deposition of shallow stoss-sided bedforms, also from a thin flow-boundary zone (Fig. 4b). The lowest U* and τ values are from when the current deposits steep stoss-sided bedforms, from a thicker flow-boundary zone (Fig. 4b). The highest U* and τ values are seen in the non-depositing current, and are higher in the basal section (Fig. 5b). There is very little overlap in U* and τ between the non-depositional and depositional phases of the current (Fig. 5a), whereas there is considerable overlap between these values during the deposition of the different bedforms.

3.3 Savage Numbers

The Savage Number (N_S) is the ratio of collisional to frictional stresses within a granular current; lower numbers show the dominance of intergranular friction as a mechanism of momentum transfer. It can be written as:

$$N_S = \frac{\left(\frac{U}{H}\right)^2 \delta^2 \rho_s}{(\rho_s - \rho_f) gH \tan\theta} \qquad \text{(Eq. 7)}$$

where δ is particle diameter, ρ_s is particle density, g is gravitational acceleration and Θ is the particle internal friction angle. Figure 6 shows the range of N_S calculated from the velocity profiles of the current during the deposition of the three bedform types, and from the non-depositional phase.

There is a decrease in N_S with increasing steepness of the bedform being deposited, which is more pronounced when looking solely at the flow-boundary zone. Here, velocity profiles in the current above planar, shallow, and steep bedforms have median N_S of 4 x 10^{-6}, 6 x 10^{-7}, and 6 x 10^{-8} respectively (Fig. 6b). The median N_S for velocity profiles from the non-depositional phase is 10^{-3}. This is higher than for any from the depositional phase, and importantly there is no overlap between the interquartile ranges of the non-depositional and depositional datasets, unlike between the three depositional datasets themselves.

4 Discussion

4.1 Velocity and shear stress profiles

The experimental granular currents follow a pattern of decreasing depth-averaged shear velocity and shear stress at one location as velocity decreases and the deposit aggrades, although there are some interesting features hidden by the depth-averaging. Shear stress, for example, typically increases downwards through the flow-boundary zone, even when velocity is consistently decreasing over the same interval (Fig. 7). This is especially evident during the deposition of planar bedforms (Fig. 5e- f). Above the flow-boundary zone, shear stress increases quasi-linearly over a short distance to τ_{max}, which is closer to the top of the flow-boundary zone than it is to U_{max} (Fig. 7).

The combination of these patterns means that shear stress is higher on average in the granular flow than the flow-boundary zone, but decreases throughout the lower granular flow, and the lowest shear stress is mostly seen in the mid-upper flow-boundary zone. At this location particles are furthest from both the static deposit and the fast upper granular flow.

The inflection point at the top of the flow-boundary zone is usually quite sharp (Fig. 7b + d), which implies poor coupling between the flow-boundary zone and the granular flow (Breard et al., 2016; Breard & Lube, 2017). In some cases the inflection point is much less sharp (Fig. 7c), suggesting low traction between the two zones. Although Figure 7c shows the velocity profile during deposition of shallow backset bedforms this behaviour is actually more common during deposition of steep bedforms, perhaps due to the overall waning of the current.

Shear velocity has been calculated for PDCs by numerous authors, although typically focusing on the dilute regime (e.g. Dellino et al., 2004; Dellino et al., 2008; Dioguardi & Dellino, 2014; Doronzo et al., 2010). The range of shear velocities derived is 0.62-3.07, considerably higher than values from this study, which range from 0.001 to 0.383. Estimates for subaqueous PDCs are 0.008-0.033 (Maeno & Imamura, 2007) and 0.022 (Doronzo & Dellino, 2010). These overlap with values from these experiments, possibly as similar to the granular currents, and unlike lofting dilute PDCs, they are denser than their surrounding fluid. Choux and Druitt (2002) suggest that shear velocity is 10-30% of average current velocity. Although meant for dilute currents the lower limit is a reasonable approximation for the whole current depth-averaged shear velocities presented here when using average velocities of 1.2, 0.4, 0.3, and 0.1 m/s for the non-depositional through to steep backset bedform depositing phases. Therefore, the shear velocities and stresses presented here are representative of dense PDCs.

4.2 Particle Segregation

The experimental granular currents and their deposits were largely homogenous in grain size distribution, with the larger particles remaining well mixed within the dominant smaller particle population. However, there is some evidence of particle segregation. Transient inverse grading is visible during the non-depositional phase (Fig. 3a), especially close to the current head (Fig. 8). Inverse grading also exists at the base of the deposit (Fig. 3b), where dominantly finer particles have been deposited (although some deposition of coarser particles forms weak stratification).

Size segregation in dense granular currents is well documented, generally forming inversely graded deposits (e.g. Gray, 2018; Iverson & Vallance, 2001; Pittari et al., 2005). This is commonly attributed to gravity-driven segregation (Baker et al., 2016; Gray 2018; Gray et al., 2015; Vallance & Savage, 2000) in the form of kinetic sieving and squeeze expulsion

(Middleton, 1970; Savage & Lun, 1988), where larger particles are forced towards the free surface, allowing the preferential deposition of smaller particles. The gravity-driven segregation that causes inverse grading is controlled by shear (Branney & Kokelaar, 2002; Bridgwater et al., 1985; Savage & Lun, 1988), so variations in the shear rate/ stress will affect the amount of vertical segregation taking place. As described in Branney and Kokelaar (2002), a decreasing shear rate, or increasing sedimentation rate, in a waning flow-boundary zone will allow progressively larger particles to deposit.

Particle segregation in the granular current may have been dampened due to the interstitial fluid. Due to the great density difference between the particles and the fluid (air), however, this effect is likely negligible (Thornton et al., 2006; Vallance & Savage, 2000). The inverse grading that is seen at the base of the deposit can be explained by unsteadiness in the current - initially high shear rates at the base of the current cause the larger particles to rise higher in the current and overpass, but as the current wanes lower shear rates (and perhaps an increasing deposition rate) prevent effective gravity-driven segregation, and deposition of both coarse and fine particles is allowed (Fig. 7 shows decreasing shear stress over time in one area of the flume).

There is also some evidence of lateral grading in the final deposit – concentrations of coarse particles are seen at the free surface towards the distal end of the deposit, presumably due to their overpassing as described above. In one experimental run a higher concentration of coarse particles upstream of the steep backset bedforms was observed – this could be an effect of the stoss-side blocking/granular jamming mechanism described in Douillet et al. (2018) and Smith et al. (2020). Alternatively this could simply represent a concentration of coarse particles in the initial sediment charge.

4.3 Deposition of bedforms

Smith et al. (2020) established that an upstream series of steepening bedforms are deposited by a rapidly defluidising granular current. Repeating those experiments here it is seen that as the current wanes and steeper bedforms are deposited, the flow-boundary zone becomes concomitantly thicker (Fig. 4b). Once deposition begins it continues as long as the current is in motion, without any pauses but at varying rates. This is different to the stepwise aggradation observed in some previous experiments (Smith et al., 2018), although this work examines a very restricted and relatively proximal area.

Profiles of concentration are not taken through this current, but particle volume fraction is uniformly high. In terms of Branney and Kokelaar's (2002) classification of flow-boundary zones, therefore, only granular-flow dominated and fluid-escape dominated are applicable. During the deposition of planar bedforms, shear is still relatively high, especially at the base of the current (Fig. 7b), resulting in a relatively thin flow-boundary zone, and it is not uncommon for the velocity gradient in the flow-boundary zone to start increasing downwards. This level of shearing increases particle-particle collisions and is recorded in the relatively high N_s (Fig. 6b). However, as mentioned above, segregation favouring the deposition of fine particles is active during this time so stratification is weak/absent. As there is relatively high shear at the base of the current and there is a clear interface between current and deposit, the flow-boundary zone during deposition of planar bedforms can be classified as granular-flow dominated (Branney & Kokelaar, 2002).

During the deposition of shallow backset bedforms shear at the base of the current has decreased as the current wanes, which also causes the cessation of the vertical segregation preventing deposition of coarse particles, resulting in relatively well-defined backset beds (Fig. 3c+d, Fig. 7c+d). Otherwise the processes are very similar as during the deposition of planar bedforms; there is not much difference in flow-boundary zone thickness (Fig. 4b), and it too could be classified as granular-flow dominated. Velocity profiles descend exponentially towards zero, and reach 1 % U_{max} relatively quickly.

When the steep backset bedforms are being deposited the current has slowed drastically due to blocking by the growing deposit, and there is no segregation of particles in the current or deposit due to the low shear (Fig. 7d). As the deposit is thick by this point it is more difficult for the upwards gas flux to reach the current and decrease frictional forces between particles. Nevertheless pore pressure is still present, as rapid deposition results in soft-sediment deformation from expulsion of the interstitial fluid. Despite the internal deformation, the lowest N_s recorded occur in this flow-boundary zone (Fig. 6b), suggesting a highly frictional regime. This all results in a deposit difficult to distinguish from the current, and the velocity profile, although already recording very small velocities, possesses a very long exponential tail before reaching 1% of U_{max}, (Fig. 7d) resulting in a very thick, sluggish flow-boundary zone (Fig. 4b). Due to the low shear, homogenous particle dispersal, and lack of a sharp interface between current and deposit, the flow-boundary zone here would be classified as fluid-escape dominated (Branney & Kokelaar, 2002). As the steep stoss-side layers seen in Smith et al. (2020) are interpreted as resulting from rapid deposition and topographic blocking rather than traction, the low levels of shear in a fluid-escape dominated flow-boundary zone support this classification.

4.4 The flow-boundary zone vs. the viscous sublayer

Figure 9 shows a remarkable correlation between the height of the top of the flow-boundary zone and the height of the top of the viscous sublayer (calculated by treating the current as clear water). These were calculated independently; the top of the flow-boundary zone by an inflection point in the velocity profile, and the top of the viscous sublayer by the point at which $Y^+ = 5$ (As a data point rarely coincides exactly with Y+ = 5 the last height at which Y+ < 5 has been used). As seen in equations (3) and (4), Y^+ is dependent on velocity, which may account for the similarity. Nevertheless, as the viscous sublayer is a concept used for clear-water channel currents it is interesting that it delineates the slower, depositing zone of a dense granular current.

The calculations show that the top of the viscous sublayer, if it existed in the experimental current, is systematically higher than the top of the flow-boundary zone. This could be because i) the top of the flow-boundary zone was underestimated and a higher inflection point should have been chosen or ii) the top of the viscous sublayer was overestimated – perhaps a larger μ should be used to account for pressurised, dusty gas. Alternatively the difference could simply be explained in that the law of the wall for the viscous sublayer is not strictly applicable to granular systems.

A much greater scatter in the data is seen for currents depositing steep bedforms than those depositing planar and shallow bedforms. As explained in both Smith et al. (2020) and section 5.4.3, the planar-shallow-steep sequence of bedforms seems to record a current increasingly dominated by frictional stresses over viscous ones. Hence, the correlation becomes more nebulous as steep backset bedforms are deposited.

5. Conclusions

The concept of the flow-boundary zone has been widely adopted in volcanology since its introduction (e.g. Brown & Andrews, 2015; Brown & Branney, 2013; Breard et al., 2015; Sulpizio & Dellino, 2008; Sulpizio et al., 2014), yet little work has been done to validate it experimentally. This study demonstrates that bedforms are not entirely restricted to traction-dominated flow-boundary zones as is commonly supposed, and that characteristics of granular-flow dominated and fluid-escape dominated flow-boundary zones are clearly seen in experimental dense granular currents.

The depositional sequence of planar-shallow-steep bedforms records the transition of the flow-boundary zone from granular-flow to fluid-escape dominated. The waning current, slowed by the steepening deposit, sees decreasing shear in the flow-boundary zone, which is manifested in decreasing effectiveness of particle size segregation. The experiments suggest that conditions in the flow-boundary zone drive the depositional behaviours as previously surmised from field studies. However, other factors must also be taken into account when interpreting deposit structure, such as the angle of the aggrading deposit and the presence of topography (Smith et al. 2020). Once deposition begins it is continuous, although unsteady, showing that these currents deposit by gradual progressive aggradation. Furthermore, the viscous law of the wall yields shear velocities for these currents which are similar to those estimated for PDCs denser than their surrounding fluid, suggesting that this is an acceptable method to investigate dense granular currents close to the wall, and that results presented here are applicable to natural PDCs. It also correlates well with the suggested method of quantitatively defining the flow-boundary zone using the velocity profile.

Acknowledgements

This work was carried out as part of a PhD project funded by a University of Hull PhD scholarship in the Catastrophic Flows Research Cluster. Experiments were performed in the Geohazards Lab at the University of Portsmouth, using equipment funded by a British Society for Geomorphology Early Career Researcher Grant held by P.R. D.P. was supported through funding from the European Research Council (ERC) under the European Union’s Horizon 2020 Research and Innovation Programme (Grant Agreement no. 72955).

Data Availability Statement

The raw velocity data taken from the high-speed video and the resulting calculations, is available at Open Science Framework via https://doi.org/10.17605/OSF.IO/S4H7W

References

Baker, J., Gray, N., & Kokelaar, P. (2016). Particle size-segregation and spontaneous levee formation in geophysical granular flows. *International Journal of Erosion Control Engineering*, *9*(4), 174–178. https://doi.org/10.13101/ijece.9.174

Branney, M.J., & Kokelaar, P. (1992). A reappraisal of ignimbrite emplacement: progressive aggradation and changes from particulate to non-particulate flow during emplacement of high grade ignimbrite. *Bulletin of* Volcanology, 54, 504–520. https://doi.org/10.1007/BF00301396

Branney, M.J., & Kokelaar, P. (2002). *Pyroclastic density currents and the sedimentation of ignimbrites*, Geological Society, London, Memoirs, 27, 143 pp. https://doi.org/10.1144/GSL.MEM.2003.027.01.02

Breard, E.C.P., Dufek, J., & Lube, G. (2017). Enhanced Mobility in Concentrated Pyroclastic Density Currents: An Examination of a Self-Fluidization Mechanism. *Geophysical Research Letters*, *45*, 654-664. https://doi.org/10.1002/2017GL075759

Breard, E.C.P., Jones, J.R., Fullard, L., Lube, G., Davies, C., & Dufek, J. (2019). The permeability of volcanic mixtures—implications for pyroclastic currents. *Journal of Geophysical Research: Solid Earth*, *124*(2), 1343–1360. https://doi.org/10.1029/2018JB016544

Breard, E.C.P., & Lube, G. (2017). Inside pyroclastic density currents—uncovering the enigmatic flow structure and transport behaviour in large-scale experiments. *Earth and Planetary Science Letters*, *458*, 22–36. https://doi.org/10.1016/j.epsl.2016.10.016

Breard, E.C.P., Lube, G., Cronin, S.J., & Valentine, G.A. (2015). Transport and deposition processes of the hydrothermal blast of the 6 August 2012 Te Maari eruption, Mt. Tongariro. *Bulletin of Volcanology*, 77(11). https://doi.org/10.1007/s00445-015-0980-5

Breard, E.C.P., Lube, G., Jones, J.R., Dufek, J., Cronin, S.J., Valentine, G.A., & Moebis, A. (2016). Coupling of turbulent and non-turbulent flow regimes within pyroclastic density currents. *Nature Geoscience*, *9*, 767–771. https://doi.org/10.1038/ngeo2794

Bridgwater, J., Foo, W.S., & Stephens, D.J. (1985). Particle mixing and segregation in failure zones-theory and experiment. *Powder Technology*, *41*(2), 147–158. https://doi.org/10.1016/0032-5910(85)87033-9

Brown, R.J., & Andrews, G.D.M. (2015). Deposits of pyroclastic density currents. In: H. Sigurdsson, B. Houghton, H. Rymer, J Stix, & S. McNutt (Eds.), *The Encyclopedia of Volcanoes* (Second Edition, pp. 631-648). Amsterdam; Academic Press. https://doi.org/10.1016/b978-0-12-385938-9.00036-5

Brown, R.J., & Branney, M.J. (2013). Internal flow variations and diachronous sedimentation within extensive, sustained, density-stratified pyroclastic density currents flowing down gentle slopes, as revealed by the internal architectures of ignimbrites on Tenerife. *Bulletin of Volcanology*, *75*(7), 1–24. https://doi.org/10.1007/s00445-013-0727-0

Calabrò, L., Esposti Ongaro, T., Giordano, G., & de' Michieli Vitturi, M. (2022). Reconstructing Pyroclastic Currents' Source and Flow Parameters From Deposit Characteristics and Numerical Modeling: The Pozzolane Rosse Ignimbrite Case Study (Colli Albani, Italy). *Journal of Geophysical Research: Solid Earth, 127(5), e2021JB023637.* https://doi.org/10.1029/2021JB023637

Calder, E.S., Cole, P.D., Dade, W.B., Druitt, T.H., Hoblitt, R.P., Huppert, H.E., et al. (1999). Mobility of pyroclastic flows and surges at the Soufriere Hills Volcano, Montserrat. *Geophysical Research Letters*, *26*, 534–540. https://doi.org/10.1029/1999GL900051

Choux, C.M., & Druitt, T.H. (2002). Analogue study of particle segregation in pyroclastic density currents, with implications for the emplacement mechanisms of large ignimbrites. *Sedimentology*, *49*(5), 907–928. https://doi.org/10.1046/j.1365-3091.2002.00481.x

Dellino, P., Isaia, R., & Veneruso, M. (2004). Turbulent boundary layer shear flows as an approximation of base surges at Campi Flegrei (Southern Italy). *Journal of Volcanology and Geothermal Research*, *133*(1–4), 211–228. https://doi.org/10.1016/S0377-0273(03)00399-8

Dellino, P., Mele, D., Sulpizio, R., La Volpe, L., & Braia, G. (2008). A method for the calculation of the impact parameters of dilute pyroclastic density currents based on deposit particle characteristics. *Journal of Geophysical Research: Solid Earth*, *113*, B07206. https://doi.org/10.1029/2007JB005365

Dioguardi, F., & Dellino, P. (2014). PYFLOW: A computer code for the calculation of the impact parameters of Dilute Pyroclastic Density Currents (DPDC) based on field data. *Computers and Geosciences*, *66*, 200–210. https://doi.org/10.1016/j.cageo.2014.01.013

Doronzo, D.M., & Dellino, P. (2010). A fluid dynamic model of volcaniclastic turbidity currents based on the similarity with the lower part of dilute pyroclastic density currents: Evaluation of the ash dispersal from ash turbidites. *Journal of Volcanology and Geothermal Research*, *191*(3–4), 193–204. https://doi.org/10.1016/j.jvolgeores.2010.01.017

Doronzo, D.M., Valentine, G.A., Dellino, P., & de Tullio, M.D. (2010). Numerical analysis of the effect of topography on deposition from dilute pyroclastic density currents. *Earth and Planetary Science Letters*, *300*(1–2), 164–173. https://doi.org/10.1016/j.epsl.2010.10.003

Douillet, G.A., Bernard, B., Bouysson, M., Chaffaut, Q., Dingwell, D.B., Gegg, L., et al. (2018). Pyroclastic dune bedforms: macroscale structures and lateral variations. Examples from the 2006 pyroclastic currents at Tungurahua (Ecuador). *Sedimentology*, *66*, 1531–1559. https://doi.org/10.1111/sed.12542

Druitt, T.H., Avard, G., Bruni, G., Lettieri, P., Maez, F. (2007). Gas retention in fine-grained pyroclastic flow materials at high temperatures. *Bulletin of Volcanology*, *69*, 881–901. https://doi.org/10.1007/s00445-007-0116-7

Farin, M., Mangeney, A., & Roche, O. (2014). Fundamental changes of granular flow dynamics, deposition, and erosion processes at high slope angles: insights from laboratory experiments. *Journal of Geophysical Research: Solid Earth*, *119*, 504–532. https://doi.org/10.1002/2013JF002750

Fisher, R.V. (1966). Mechanism of deposition from pyroclastic flows. *American Journal of Science, 264*(5), 350-363. https://doi.org/10.2475/ajs.264.5.350

Forterre, Y., & Pouliquen, O. (2008). Flows of dense granular media. *Annual Review of Fluid Mechanics, 40*(1), 1–24. https://doi.org/10.1146/annurev.fluid.40.111406.102142

GDR MiDi (2004). On dense granular flows. *European Physical Journal E, 14*(4), 341–365. https://doi.org/10.1140/epje/i2003-10153-0

Geldart, D. (1973). Types of gas fluidization. *Powder Technology, 7*, 285–292. https://doi.org/10.1016/0032-5910(73)80037-3

Girolami, L., Roche, O., Druitt, T., & Corpetti, T. (2010). Particle velocity fields and depositional processes in laboratory ash flows, with implications for the sedimentation of dense pyroclastic flows. *Bulletin of Volcanology, 72*, 747–759. https://doi.org/10.1007/s00445-010-0356-9

Gray, J.M.N.T. (2018). Particle segregation in dense granular flows. *Annual Review of Fluid Mechanics*, *50*(1), 407–433. https://doi.org/10.1146/annurev-fluid-122316-045201

Gray, J.M.N.T., Gajjar, P., & Kokelaar, P. (2015). Particle-size segregation in dense granular avalanches. *Comptes Rendus Physique, 16*(1), 73–85. https://doi.org/10.1016/j.crhy.2015.01.004

Hayashi, J., & Self, S. (1992). A comparison of pyroclastic flow and debris avalanche mobility. *Journal of Geophysical Research, 97*, 9063–9071. https://doi.org/10.1029/92JB00173

Iverson, R.M., & Vallance, J.W. (2001). New views of granular mass flows. *Geology*, *29*(2), 115–118. https://doi.org/10.1130/0091-7613(2001)029<0115:NVOGMF>2.0.CO

Jessop, D.E., Hogg, A.J., Gilbertson, M.A., & Schoof, C. (2017). Steady and unsteady fluidised granular flows down slopes. *Journal of Fluid Mechanics, 827*, 67–120. https://doi.org/10.1017/jfm.2017.458

Lube, G., Breard, E.C.P., Jones, J., Fullard, L., Dufek, J., Cronin, S.J., & Wang, T. (2019). Generation of air lubrication within pyroclastic density currents. *Nature Geoscience, 12*, 381–386. https://doi.org/10.1038/s41561-019-0338-2

Lube, G., Cronin, S.J., Platz, T., Freundt, A., Procter, J.N., Henderson, C., & Sheridan, M.F. (2007). Flow and deposition of pyroclastic granular flows: A type example from the 1975 Ngauruhoe eruption, New Zealand. *Journal of Volcanology and Geothermal Research, 161*(3), 165–186. https://doi.org/10.1016/j.jvolgeores.2006.12.003

Maeno, F., & Imamura, F. (2007). Numerical investigations of tsunamis generated by pyroclastic flows from the Kikai caldera, Japan. *Geophysical Research Letters, 34*(23), 1–5. https://doi.org/10.1029/2007GL031222

Mangeney, A., Roche, O., Hungr, O., Mangold, N., Faccanoni, G., & Lucas, A. (2010). Erosion and mobility in granular collapse over sloping beds. *Journal of Geophysical Research: Earth Surface*, *115*(3), 1–21. https://doi.org/10.1029/2009JF001462

Middleton, G.V. (1970). Experimental studies related to problems of flysch sedimentation. In: J. Lajoie (Ed.) *Flysch Sedimentology in North America, Geological Association of Canada Special Paper* (Vol. 7, pp. 253-272). Toronto: Business and Economic Service Ltd.

Montserrat, S., Tamburrino, A., Roche, O., & Niño, Y. (2012). Pore fluid pressure diffusion in defluidizing granular columns. *Journal of Geophysical Research, 117*, F02034. https://doi.org/10.1029/2011JF002164

Pittari, A., Cas, R.A.F., & Martí, J. (2005). The occurrence and origin of prominent massive, pumice-rich ignimbrite lobes within the Late Pleistocene Abrigo Ignimbrite, Tenerife, Canary Islands. *Journal of Volcanology and Geothermal Research, 139*(3–4), 271–293. https://doi.org/10.1016/j.jvolgeores.2004.08.011

Pollock, N.M., Brand, B.D., Rowley, P.J., Sarocchi, D., & Sulpizio, R. (2019). Inferring pyroclastic density current flow conditions using syn-depositional sedimentary structures. *Bulletin of Volcanology, 81*, 46. https://doi.org/10.1007/s00445-019-1303-z

Roche, O. (2012). Depositional processes and gas pore pressure in pyroclastic flows: an experimental perspective. *Bulletin of Volcanology, 74*, 1807–1820. https://doi.org/10.1007/s00445-012-0639-4

Roche, O., Gilbertson, M.A., Phillips, J.C., & Sparks, R.S.J. (2004). Experimental study of gas-fluidized granular flows with implications for pyroclastic flow emplacement. *Journal of Geophysical Research: Solid Earth, 109*, B10201. https://doi.org/10.1029/2003JB002916

Roche, O., Gilbertson, M.A., Phillips, J.C., & Sparks, R.S.J. (2006). The influence of particle size on the flow of initially fluidised powders. *Powder Technology, 166*(3), 167–174. https://doi.org/10.1016/j.powtec.2006.05.010

Roche, O., Montserrat, S., Niño, Y., & Tamburrino, A. (2010). Pore fluid pressure and internal kinematics of gravitational laboratory air-particle flows: insights into the emplacement dynamics of pyroclastic flows. *Journal of Geophysical Research: Solid Earth, 115*, B12203. https://doi.org/10.1029/2009JB007133

Rowley, P., Giordano, G., Silleni, A., Smith, G.M., Trolese, M., & Williams, R. (2023). Stationary surface waves and antidunes in dense pyroclastic density currents. *EarthArXiv*. https://doi.org/10.31223/X5TW8V

Rowley, P.J., Roche, O., Druitt, T.H., & Cas, R. (2014). Experimental study of dense pyroclastic density currents using sustained, gas-fluidized granular flows. *Bulletin of Volcanology, 76*, 855. https://doi.org/10.1007/s00445-014-0855-1

Savage, S.B., & Lun, C.K. (1988). Particle size segregation in inclined chute flow of dry cohesionless granular solids. *Journal of Fluid Mechanics, 189*(1), 311-335. https://doi.org/10.1017/S002211208800103X

Sarno, L., Carravetta, A., Tai, Y.C., Martino, R., Papa, M.N., & Kuo, C.Y. (2018). Measuring the velocity fields of granular flows – Employment of a multi-pass two-dimensional particle image velocimetry (2D-PIV) approach. *Advanced Powder Technology, 29*(12), 3107–3123. https://doi.org/10.1016/j.apt.2018.08.014

Sulpizio, R., & Dellino, P. (2008). Depositional mechanisms and pulsating behaviour of pyroclastic density currents. In: L. Marti & J. Gottsman (Eds.), *Caldera volcanism: analysis, modelling and response, Developments in Volcanology* (Vol. 10, pp 57-96). Elsevier, Amsterdam. https://doi.org/10.1016/S1871-644X(07)00002-2

Sulpizio, R., Dellino, P., Doronzo, D.M., & Sarocchi, D. (2014). Pyroclastic density currents: State of the art and perspectives. *Journal of Volcanology and Geothermal Research, 283*, 36–65. https://doi.org/10.1016/j.jvolgeores.2014.06.014

Smith, G., Rowley, P., Williams, R., Giordano, G., Trolese, M., Silleni, A., et al. (2020). A bedform phase diagram for dense granular currents. *Nature Communications*, *11*, 2873. https://doi.org/10.1038/s41467-020-16657-z

Smith, G.M., Williams, R., Rowley, P.J., & Parsons, D.R. (2018). Investigation of variable aeration of monodisperse mixtures: implications for pyroclastic density currents. *Bulletin of Volcanology*, *80*, 67. https://doi.org/10.1007/s00445-018-1241-1

Smith, G.M., Williams, R., Rowley, P., & Parsons, D. (2023). Characterising the flow-boundary zone in fluidised granular currents [dataset]. Open Science Framework. https://doi.org/10.17605/OSF.IO/S4H7W

Southard, J.B. (2006). Flow in channels. In: Introduction to fluid motions, sediment Transport, and current-generated sedimentary structures. Massachusetts Institute of Technology: MIT OpenCourseWare. Retrieved from: https://ocw.mit.edu/courses/12-090-introduction-to-fluid-motions-sediment-transport-and-current-generated-sedimentary-structures-fall-2006/pages/course-textbook/

Taberlet, N., Richard, P., Valance, A., Losert, W., Pasini, J.M., Jenkins, J.T., & Delannay, R. (2003). Superstable granular heap in a thin channel. *Physical Review Letters, 91*(26), 1–4. https://doi.org/10.1103/PhysRevLett.91.264301

Thielicke, W. (2014). The flapping flight of birds - analysis and application (Doctoral dissertation). Retrieved from https://research.rug.nl/en/publications/the-flapping-flight-of-birds-analysis-and-application. Groningen, Netherlands: Rijksuniversiteit Groningen. http://irs.ub.rug.nl/ppn/382783069

Thielicke, W., & Stamhuis, E.J. (2014). PIVlab – towards user-friendly, affordable and accurate digital particle image velocimetry in MATLAB. *Journal of Open Research Software*, *2*(1):e30. http://dx.doi.org/10.5334/jors.bl

Thornton, A.R., Gray, J.M.N.T., & Hogg, A.J. (2006). A three-phase mixture theory for particle size segregation in shallow granular free-surface flows. *Journal of Fluid Mechanics*, *550*, 1–25. https://doi.org/10.1017/S0022112005007676

Vallance, J.W., & Savage, S.B. (2000). Particle segregation in granular flows down chutes. In: Rosato, A., & Blackmore, D. (Eds.), Segregation in granular flows (International Union of Theoretical and Applied Mechanics symposium): Dordrecht, Netherlands, 31–51. https://doi.org/10.1007/978-94-015-9498-1_3

Wang, N., Lu, H., Xu, J., Guo, X., & Liu, H. (2019). Velocity profiles of granular flows down an inclined channel. *International Journal of Multiphase Flow, 110*(I), 96–107. https://doi.org/10.1016/j.ijmultiphaseflow.2018.09.002

Wohletz, K.H. (1998). Pyroclastic surges and compressible two-phase flow. In: A. Freundt, & M. Rosi (Eds.), *From magma to tephra: modelling physical processes of explosive volcanic eruptions, Developments in Volcanology* (Vol. 4, pp. 247-312). https://doi.org/10.1016/S1871-644X(01)80008-5

Zrelak, P.J., Pollock, N.M., Brand, B.D., Sarocchi, D., & Hawkins, T. (2020). Decoding pyroclastic density current flow direction and shear conditions in the flow boundary zone via particle-fabric analysis. *Journal of Volcanology and Geothermal Research, 402*, 106978. https://doi.org/10.1016/j.jvolgeores.2020.106978

Tables

Table 1

Terms, symbols, and definitions used in this paper.

Term/symbol	**Definition**
Flow-boundary zone	Zone of the velocity profile bounded by the top of the static deposit at the bottom and the transition to a linear velocity profile at the top.
Free Surface	Top surface of the Granular Flow.
g	Gravitational acceleration.
Granular Flow	Zone of the velocity profile bounded by the transition from flow-boundary zone to linear at the bottom, and the free surface at the top.
H	Thickness of the current, from the base to the free surface.
(H-Y')/H	Height in the current as proportion of H.
N_S	Savage number. Defined as $\frac{\rho_s\left(\frac{U}{H}\right)^2\delta^2}{(\rho_s-\rho_f)gHtan\theta}$.
Re	Reynolds number. Defined as $Re = \frac{U\rho H}{\mu}$.
Static deposit	Area between the flume base and the current base.
Top of the static deposit/current base	Height at which U = 1% U_{max}.
U	Velocity.
U_{max}	Maximum velocity below the free surface.
U_{mf_st}	Static minimum fluidisation velocity.
U^+	Dimensionless velocity. Defined as U/U*.
U*	Shear velocity. Defined as $\sqrt{\frac{U\mu_f}{Y\rho_f}}$.
V	Kinematic viscosity. Defined as $\mu f/\rho_f$.
Viscous Sublayer	Area between Y^+ 0 and 5.
Y	Distance above current base.
Y'	Distance below free surface.
Y^+	Dimensionless distance from current base. Defined as $(\rho_f U^* Y)/\mu$.
δ	Particle diameter.
Θ	Particle internal friction angle.

Θ_{Dyn}	Dynamic angle of repose.
μ	Bulk dynamic viscosity.
μ_f	Fluid dynamic viscosity.
ρ	Bulk density.
ρ_f	Fluid density.
ρ_s	Particle density.
τ	Shear stress. Defined as ${U^*}^2\rho_f$
τ_{max}	Maximum shear stress below the free surface.

Figures

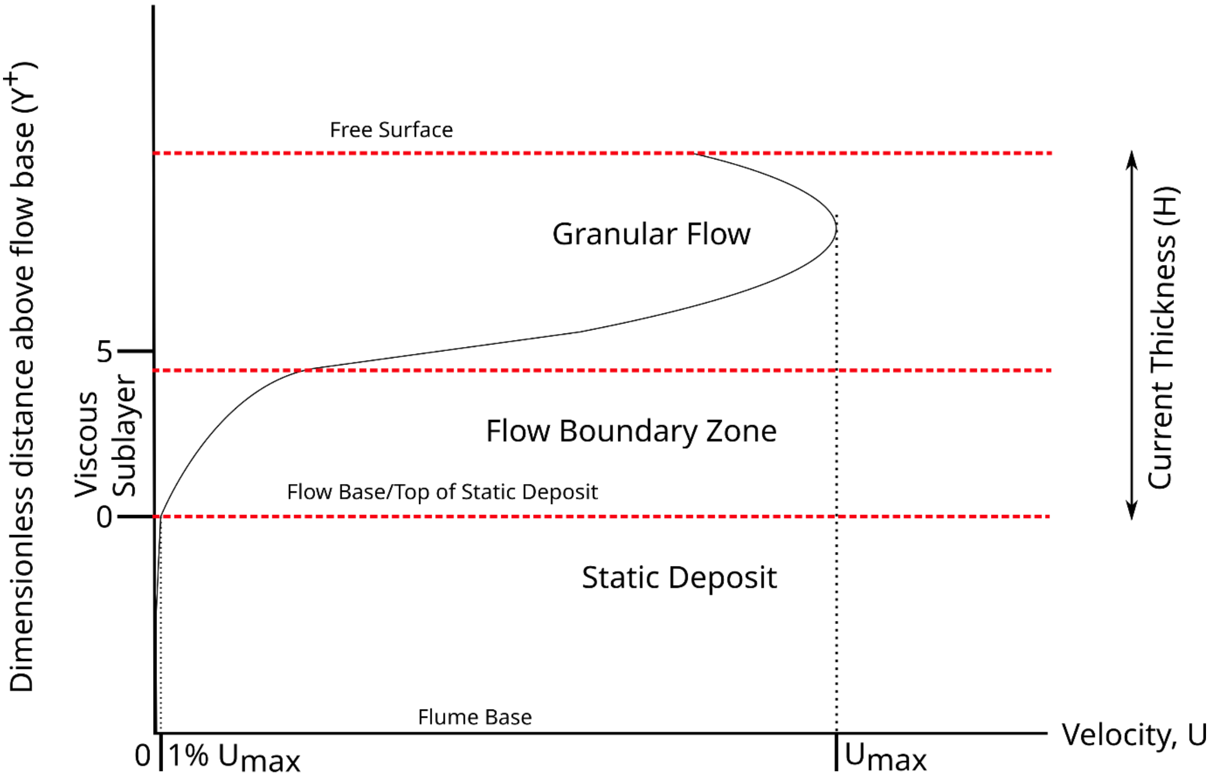

Figure 1 Schematic diagram of a velocity profile through a typical dense granular current. The profile is synthesised from various experiments (Taberlet et al., 2003; GDR MiDi, 2004; Girolami et al., 2010). See Table 1 for definitions.

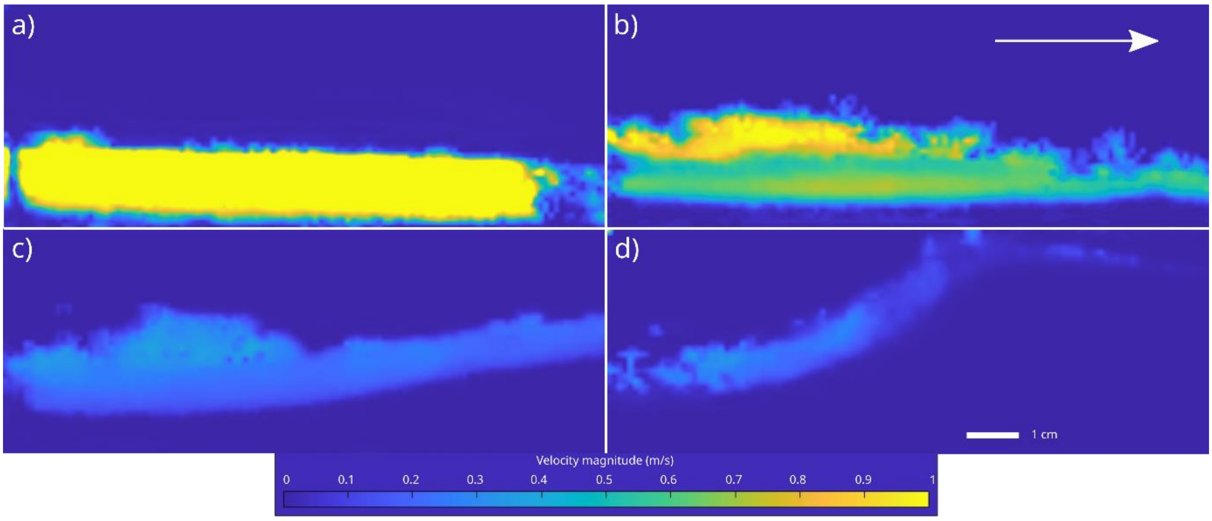

Figure 2 Representative velocity field for various phases of the experimental granular current. **a** Non depositional phase. **b** During deposition of planar bedforms. **c** During deposition of shallow stoss-side bedforms. **d** During deposition of steep stoss-side bedforms. Note that velocities greater than 1 m/s are not shown here.

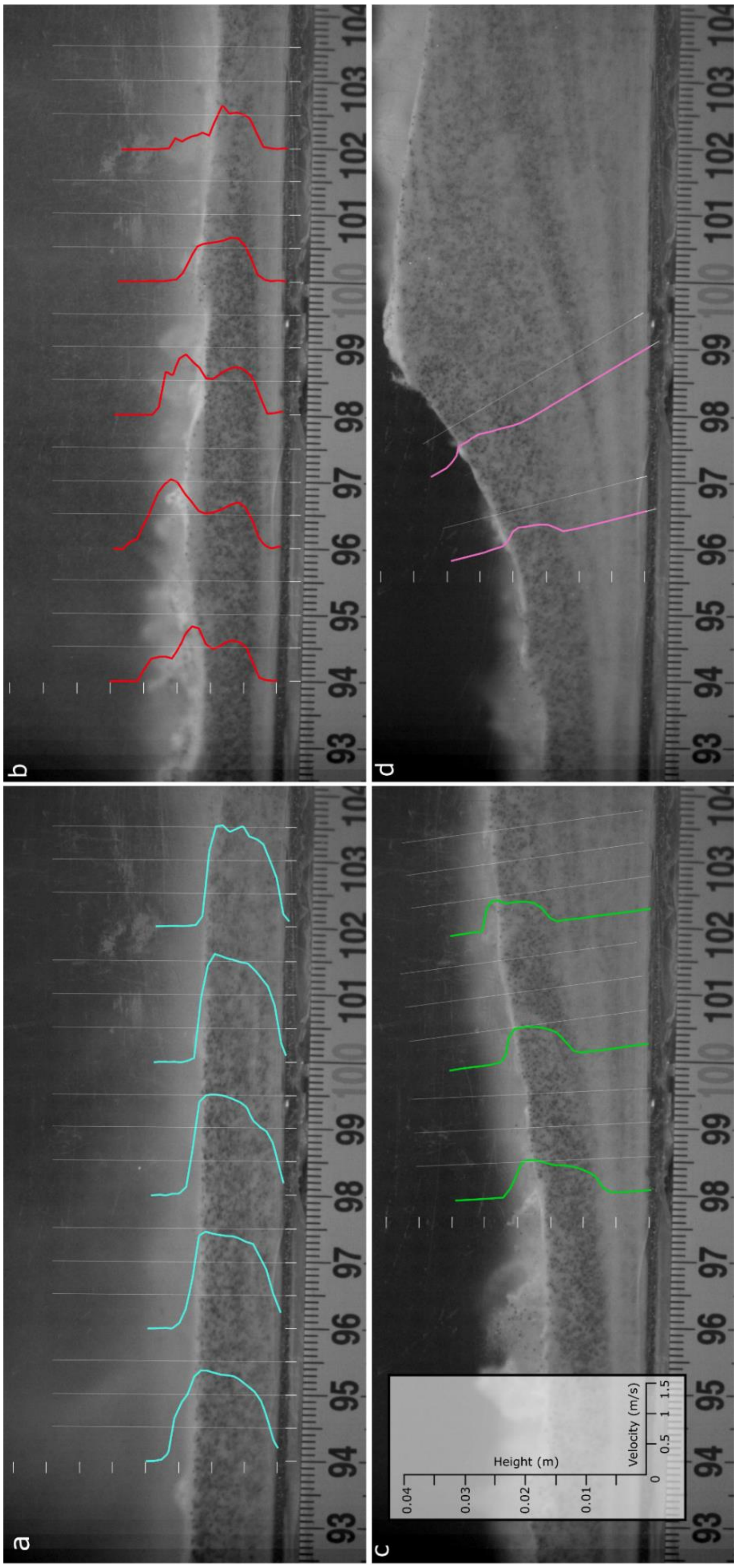

Figure 3 Snapshots of a granular current at different phases of its evolution, with velocity profiles superimposed on top, perpendicular to flow direction. **a** Non-depositional phase **b** Depositing planar bedforms **c** Depositing shallow stoss-side bedforms **d** Depositing steep stoss-side bedforms. Velocity intervals are 0.5 m/s and height intervals are 0.005 m, as seen on inset example. Height is above the flume base.

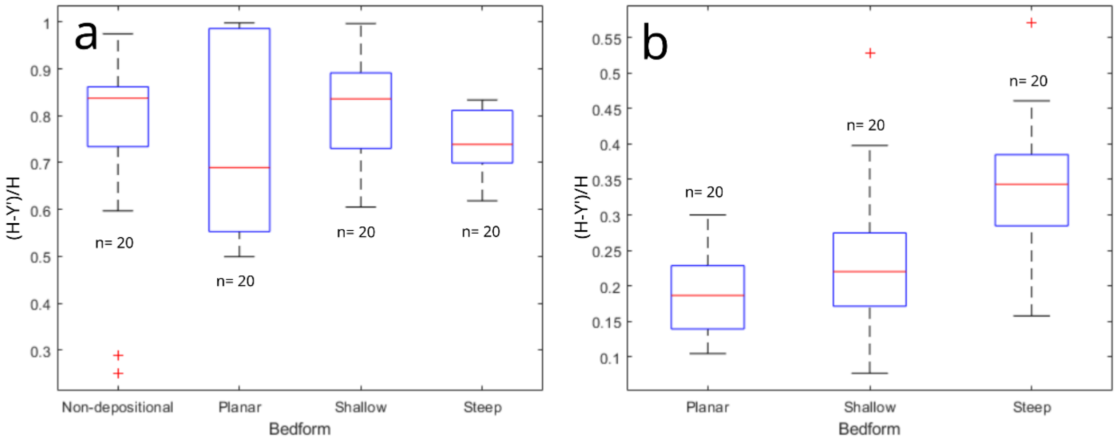

Figure 4 a Box plot showing the position U_{max} as a proportion of current thickness, or (H-Y')/H, for different depositional phases of the current. Red line is the median, blue box is the interquartile range. Dashed lines indicate values less than the 1st quartile or greater than the 3rd quartile, and red crosses are outliers. **b** Box plot showing the position of the top of the flow-boundary zone as (H-Y')/H (and so its dimensionless thickness) for currents depositing different bedforms.

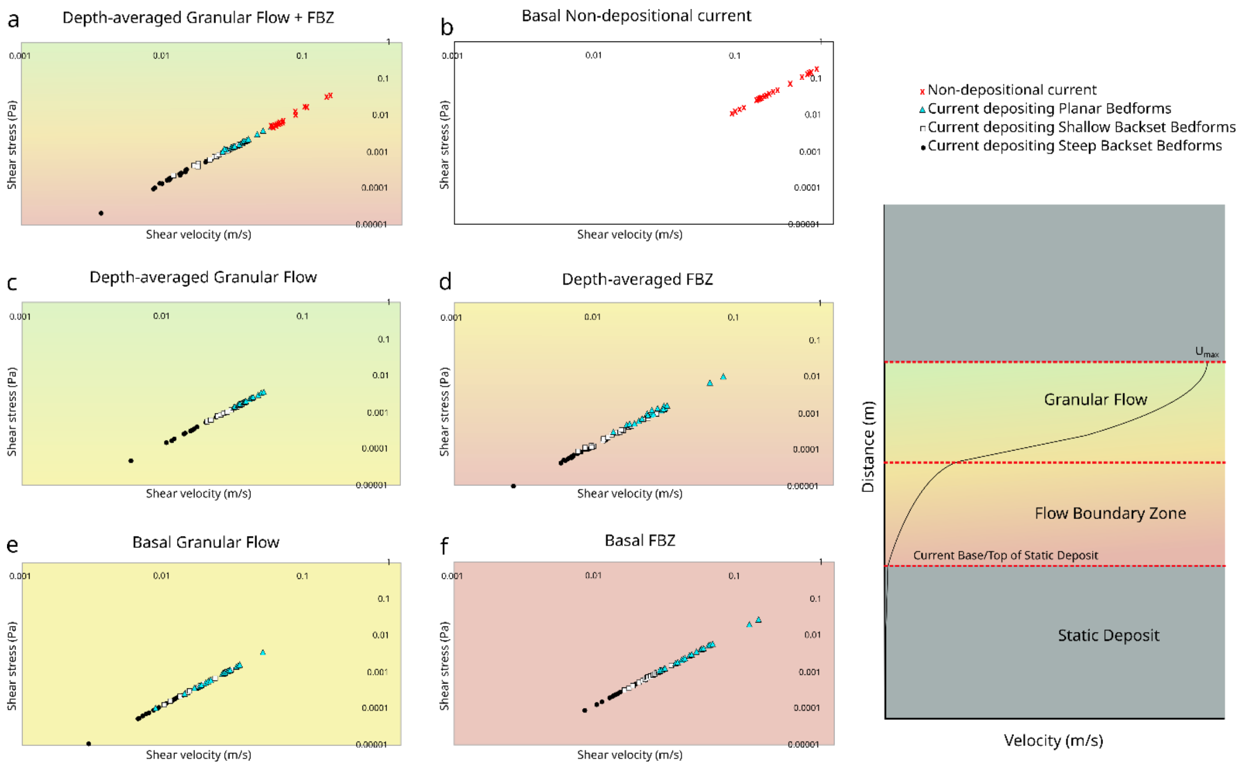

Figure 5 Shear velocity and shear stress values for an experimental current. Each data point represents either a single depth-averaged velocity profile or the basal point of a velocity profile. 20 velocity profiles were examined for each depositional phase (non-depositional, planar bedforms, shallow backset bedforms, and steep backset bedforms). Shear velocity and shear stress decrease as steeper bedforms are deposited. **a** shows the values depth-averaged through the whole current. **b** shows the values at the base of the current while it is non-depositional. **c** shows the values depth-averaged through the granular flow part of the current only. **d** shows the values at the base of the granular flow part of the current only. **e** shows the values depth-averaged through the flow-boundary zone. **f** shows the values at the base of the flow-boundary zone. **g** is a modified version of Figure 1 showing the location on the velocity profile (of a depositing granular current) of the previous plots.

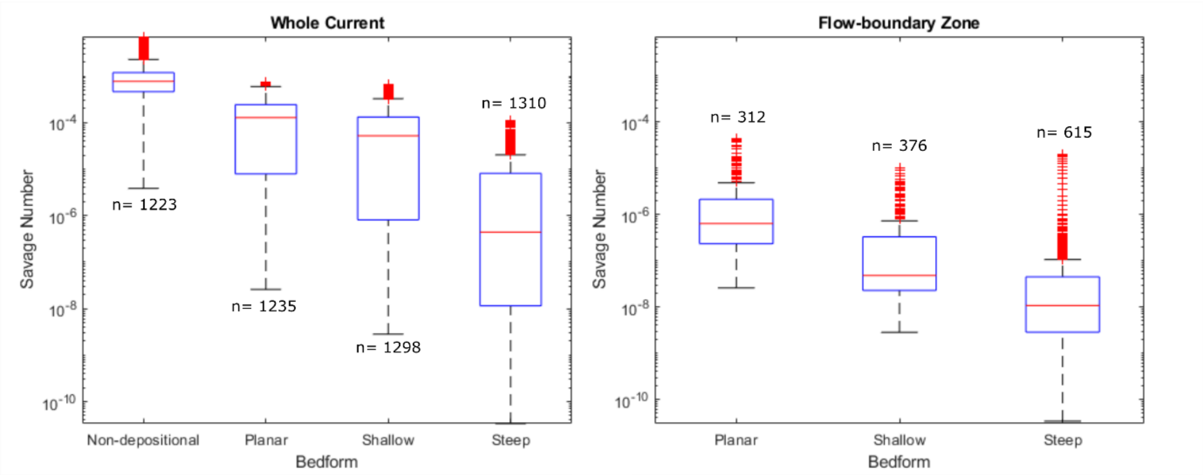

Figure 6 Box plots showing the ranges of Savage Numbers for the experimental current when depositing different bedforms and for the non-depositional current. **a** Through the whole current, including the flow-boundary zone. **b** Through the flow-boundary zone only. Red line is the median, blue box is the interquartile range. Dashed lines indicate values less than the 1st quartile or greater than the 3rd quartile, and red crosses are outliers.

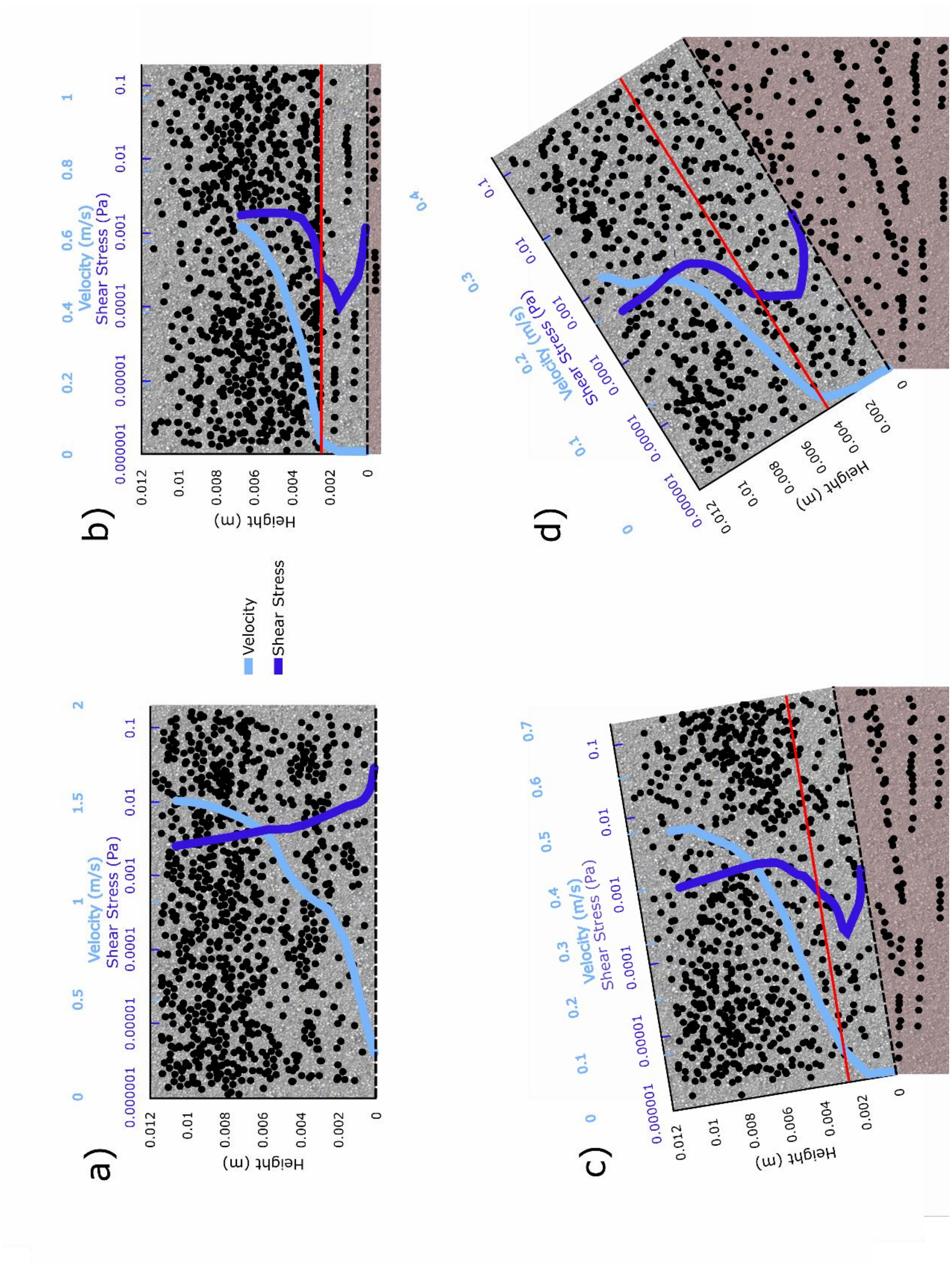

Figure 7 Schematic figures and representative velocity (pale blue) and shear stress (dark blue) profiles for the **a** non-depositional phase, deposition of **b** planar beds **c** shallow stoss-sided bedforms **d** steep stoss-sided bedforms. Height is from the current base to U_{max}. These profiles are from the same snapshots seen in Figure 2 (a = 98 cm, b = 94 cm, c = 100 cm, d = 96 cm). The top of the flow-boundary zone is marked by a red line. Black dots represent the coarser particle fraction. Grey stipple is the moving current and mauve stipple the static deposit. Note different velocity scales.

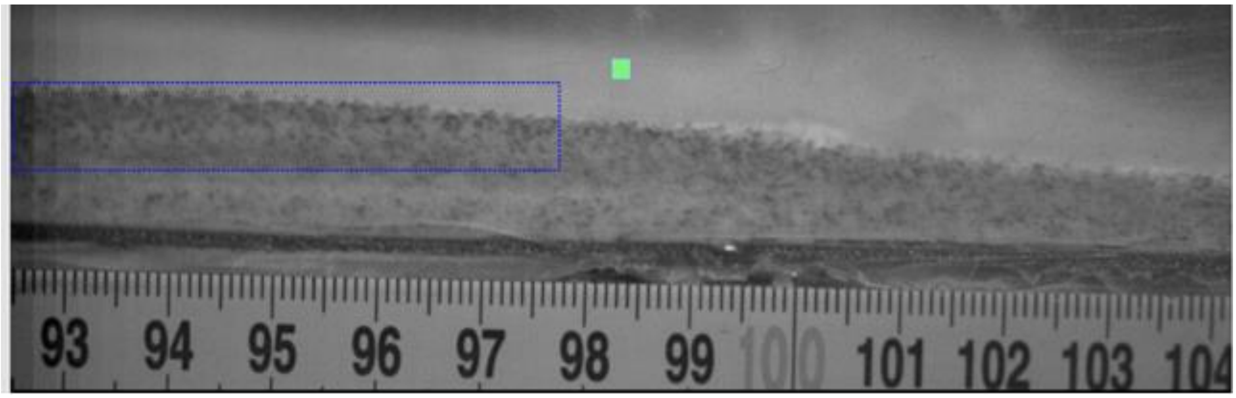

Figure 8 Transient inverse grading during the non-depositional phase. Blue box highlights the greater concentration of coarser particles, compared to lower in the current. This snapshot is close behind the current head, off view to the right.

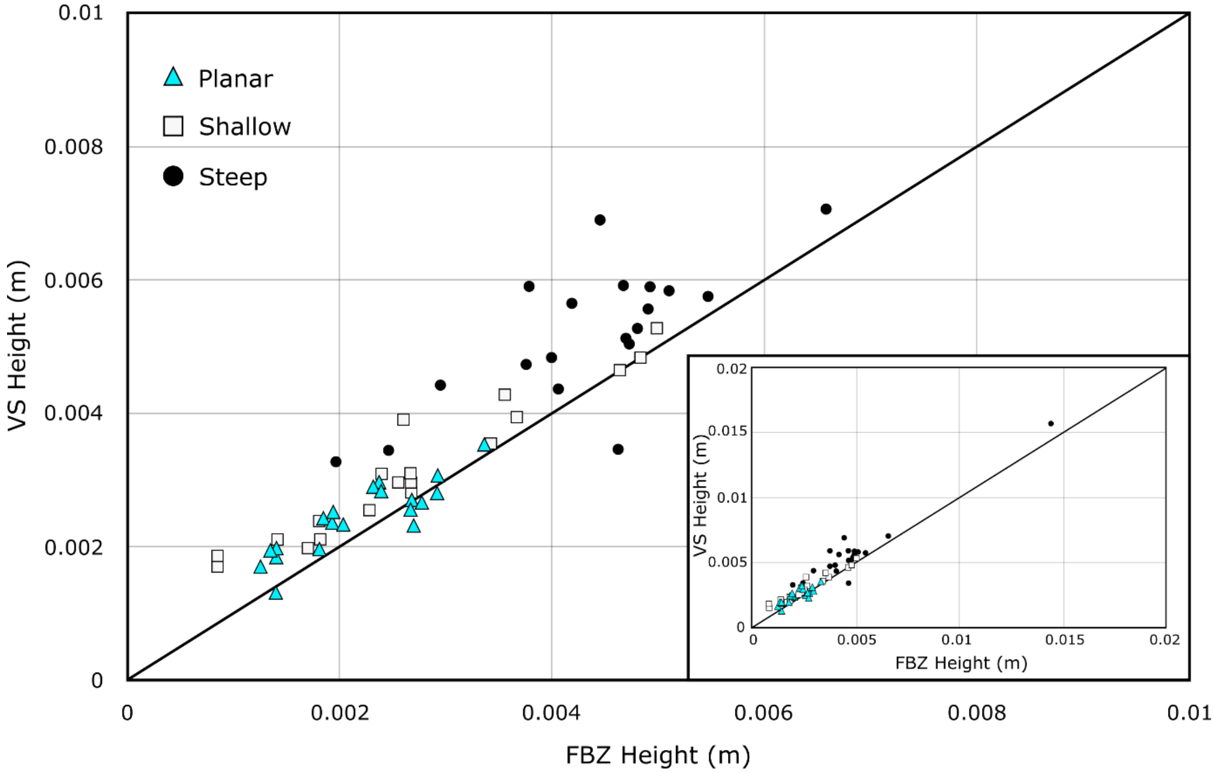

Figure 9 Correlation between the height of the top of the viscous sublayer and the height of the top of the flow-boundary zone for the current as various bedforms are deposited. Inset shows outlier in the top right.